frontiers in Materials

ORIGINAL RESEARCH
published: 29 July 2021
doi: 10.3389/fmats.2021.652009

Ceramics From Ti-Extraction Blast Furnace Slag and Their Crystalline Phase, Microstructure, and Photocatalytic Performance

Hao You[1,2,3], *Hongjuan Sun*[1,2,3]*, *Yao Li*[1,2,3] *and Tongjiang Peng*[2,3]

[1] School of Environment and Resource, Southwest University of Science and Technology, Mianyang, China, [2] Education Ministry Key Laboratory of Solid Waste Treatment and Resource Recycle, Southwest University of Science and Technology, Mianyang, China, [3] Institute of Mineral Materials and Application, Southwest University of Science and Technology, Mianyang, China

To solve the environmental problems caused by the deposition of Ti-extraction blast furnace slag (EBFS) and to develop the functionality of the slag ceramics, photocatalytic EBFS ceramics were prepared via powder sintering at different temperatures. The phase composition dramatically changed in ceramics sintered at 1,000–1,150°C, but remained constant in samples treated at 1,150–1,200°C, just revealing the variations in the relative content of each phase. The photocatalytic performance of the samples was assessed through the catalytic degradation of Rhodamine B (RhB). Furthermore, it was shown to strongly depend on the relative Fe-bearing diopside content, achieving a maximum in EBFS-1180 ceramic. In this ceramic, the Fe-bearing diopside was found to degrade up to 77% of RhB under UV light irradiation at pH = 2, and its acid corrosion ratio after 24 h was only 0.03%, indicating that EBFS-1180 ceramic had the ability to degrade pollutants in an acidic environment.

Keywords: Ti-extraction blast furnace slag, ceramics, crystalline phase, microstructure, photocatalytic performance

OPEN ACCESS

Edited by:
Rajesh Adhikari,
Université du Québec, Canada

Reviewed by:
Changzheng Hu,
Guilin University of Technology, China
David Olubiyi Obada,
Ahmadu Bello University, Nigeria

***Correspondence:**
Hongjuan Sun
sunhongjuan@swust.edu.cn

Specialty section:
This article was submitted to Ceramics and Glass, a section of the journal Frontiers in Materials

Received: *11 January 2021*
Accepted: *06 April 2021*
Published: *29 July 2021*

Citation:
You H, Sun H, Li Y and Peng T (2021) Ceramics From Ti-Extraction Blast Furnace Slag and Their Crystalline Phase, Microstructure, and Photocatalytic Performance. Front. Mater. 8:652009. doi: 10.3389/fmats.2021.652009

INTRODUCTION

Huge deposits of titanium-bearing blast furnace slag (TBBFS), exceeding 60 million tons at the yearly increase of 3 million tons, have been discovered in the Panxi region of China (Lei et al., 2018). In order to reduce landfills and recover titanium resources, the current solution is to extract titanium from the slag via the "high temperature carbonization–low temperature chlorination" technology. For this, the titanium component is first carbonized to TiC at a high temperature and then reacted with Cl_2 to form gaseous $TiCl_4$ at a low temperature, allowing one to effectively extract more than 70% of titanium (He et al., 2019a). Meanwhile, this method also results in a secondary industrial waste slag, the so-called Ti-extraction blast furnace slag (EBFS) (He et al., 2019b) or chlorine-containing low-titanium slag (CTS) (You et al., 2020). At present, the annual output of EBFS is continuously increasing, approaching 100,000 tons (Zhang et al., 2018). The CTS includes about 2–5 wt% of Cl, making it difficult to be directly used as a building material, and 8–10 wt% of TiO_2, leading to serious environmental problems. One effective way of large-scale consumption and utilization of EBFS is employing them as raw materials for building materials industry, e.g., in the form of foam concretes, cementitious materials, and foam glass-ceramics. In this respect,

Zhang et al. (2018, 2019) took EBFS and red gypsum as the main raw materials to prepare foam concretes and cementitious materials, whose mechanical properties met the requirements of relevant standards. Xi et al. (2018, 2020) used EBFS and waste glass to produce the low-density and high-porosity foam glass ceramics. The effects of heat treatment conditions and slag ratio on the microstructure and characteristics of foam glass-ceramics were investigated, as well.

The roasted TBBFS is composed of phases such as gehlenite, akermanite, diopside, and perovskite, which are favorable to degrade organic dyes and reduce heavy metal ions. Yang et al. (2004) applied the roasted TBBFS as the photocatalyst to degrade methylene blue (MB) and found that the degradation efficiency was closely related to the solution's pH, being the highest in the acidic medium. Lei and Xue (2008a) prepared perovskite-type photocatalysts from TBBFS and used them to reduce Cr(VI), showing that the rate of Cr(VI) reduction mainly depends on the perovskite/anatase ratio. Lei and Xue (2008b) also made attempts to reduce Cr(VI) by applying sulfate-modified TBBFS and demonstrated that the high $m(CaTiO_3)/m(TiO_2)$ ratio and the increase in surface acidity could effectively improve the reduction efficiency. Hou et al. (2020) prepared the formic acid-modified TBBFS photocatalysts by a mechanochemical method and proved that increasing specific surface area and surface acidity of the photocatalysts were the main reasons for the catalytic reduction of NO. Fe^{3+} doping leads to the lattice distortion of diopside, resulting in excellent photocatalytic activity of Fe-doped diopside. For instance, Yang et al. (2012) found that embedding Fe dopants in the amount of 1.848% into diopside ensured a significant photocatalytic activity and up to 95% degradation of MB. Currently, TBBFS is being roasted and modified through inorganic acid treatment or metal doping to better explore its photocatalytic performance. However, there is still no data on the EBFS-based ceramics and their photocatalytic performance. Due to a similar chemical composition of TBBFS and EBFS, diopside and perovskite will be formed in EBFS after heat treatment, which makes EBFS-based ceramics have the photocatalytic performance.

In this respect, the present work aims to produce EBFS ceramics using the powder sintering method and evaluate their photocatalytic performance via the catalytic degradation of RhB. Particular attention is paid to a thorough analysis of the relationships between the phase, microstructural characteristics and the photocatalytic performance of EBFS ceramics.

EXPERIMENT

Raw Material

Ti-extraction blast furnace slag was obtained from the Panzhihua deposit, China. The chemical composition of EBFS is mainly presented by CaO, SiO_2, and Al_2O_3, with contents of 28.30, 24.18, and 11.66%, respectively. Besides, EBFS contains certain amounts of TiO_2, MgO, Fe_2O_3, and Cl (7.57, 6.65, 3.83, and 2.58%, respectively). Moreover, the presence of chloride in EBFS leads to a strong moisture absorption, resulting in the water concentration of 5.28% (You et al., 2020). The main chemical composition of EBFS is similar to that of calcium–silicon-based ceramics, where TiO_2 and Fe_2O_3 favor their crystallization (Rezvani et al., 2005; Zhao et al., 2014).

Preparation of EBFS Ceramics

Ti-extraction blast furnace slag was put into an oven and exposed to 24 h of heating at 105 ± 5°C. After drying, the slag was balled for 10 h and passed through a 300-mesh sieve (<47 μm). The fine powder was placed into molds and pressed for 10–15 s under a pressure of 6 MPa to obtain Ø 25.3 mm × 5.5 mm cylindrical disks and 50 mm × 5 mm × 5 mm rectangular bars as green bodies. Disks and bars were then left in a furnace for heating from room temperature to 1,000, 1,100, 1,150, 1,180, and 1,200°C at the rate of 5°C/min and kept at the final temperature for 1 h. The naturally cooled EBFS ceramic samples were labeled as EBFS-t, where t was the final sintering temperature.

Characterization and Performance Testing

Sample Characterization

The phase composition of EBFS ceramics was examined by X-ray diffraction using an Ultima IV X-ray diffractometer (Rigaku, Japan) in Cu Kα radiation at operating conditions of 40 kV, 40 mA. The X-ray powder diffraction (XRD) profiles were recorded in a 2θ range from 10 to 80° at a scanning speed of 4°/min and a scan step of 0.02°.

The Whole Pattern Fit module in JADE protocol was used for the quantitative analysis and structural refinement of phases in accordance with a procedure provided in Zhao and Tan (2018). For this, the background curve was described by the 5th-order polynomial, the XRD profile shape was fitted by a pseudo-Voigt function, and the refinement range was 2θ = 10–80°. The refinement quality was assessed from the R-to-E-factor (R/E) ratio as the "goodness-of-fit" indicator: the closer it was to 1, the better was the fit (Wang et al., 2010).

The microstructure and elemental distribution of EBFS ceramics were inspected by scanning electron microscopy using a Sigma300 microscope (Carl Zeiss, Germany) equipped with an energy dispersive spectrometer (EDS). The optical absorbance of EBFS ceramic samples was evaluated by means of a Solidspec-3700 diffusive reflectance spectrometer (Shimadzu, Japan). The solution absorbance was measured by an Evolution 300 UV-visible (UV-Vis) spectrophotometer (Thermo Scientific, United States).

Acid Resistance

Ti-extraction blast furnace slag-1180 sample was immersed in an acidic solution with pH = 2 for 24 h. The acid corrosion rate was calculated as follows:

$$\omega = \frac{M_1 - M_2}{M_1} \times 100\% \quad (1)$$

where ω is the acid corrosion rate (%), M_1 is the sample mass before immersion (g), and M_2 is the sample mass after immersion (g).

Photocatalytic Performance

The photocatalytic performance of the prepared ceramics was evaluated using the two following methods.

(1) RhB was selected as the catalytic degradation solution, and the UV lamp was used as the light source. EBFS ceramics were crushed and passed through a 300-mesh sieve. Each powder was then took in a quantity of 0.05 g and placed in 100 mL of the RhB solution (20 mg/L); the solutions were placed on a magnetic stirrer 1 h with no light source under room temperature to reach adsorption balance, and then, the solutions were subjected to different time intervals of the UV light irradiation and left for natural sedimentation within 24 h. After that, the upper layers were recovered, and their absorbance was measured via the UV-Vis absorption spectroscopy at 554 nm. The degradation rate of RhB (%) was calculated as follows:

$$D = \frac{A_0 - A_t}{A_0} = \frac{C_0 - C_t}{C_0} \quad (2)$$

where D is the degradation rate of RhB (%); A_0 and A_t are the absorbance values of the upper layer at 554 nm after the dark adsorption experiments and light irradiation, respectively; C_0 and C_t are the RhB concentrations before and after degradation, respectively (mg/L) (Li et al., 2019).

(2) EBFS-1180 sample was soaked in 20 mL of the RhB solution (20 mg/L) with pH = 2.0 and dried in the dark. After that, the sample was subjected to the UV light irradiation and no light irradiation. The color change of the RhB layer was monitored in the BX051 microscope (Olympus, Japan) every 20 min. The lighter was the RhB layer, the higher was its degradation rate (Zhang et al., 2017).

Physical Properties

The bulk density and water absorption of EBFS ceramics were measured by the Archimedes method using an electronic analytic balance (WT5003GHS, WANT, China). The linear shrinkage rates of ceramic samples were calculated by Eq. 3:

$$\eta = \frac{L_1 - L_2}{L_1} \times 100\% \quad (3)$$

where η is the linear shrinkage rate (%), L_1 is the diameter of cylindrical disk (mm), and L_2 is the diameter of ceramic sample (mm).

The bending strength of EBFS ceramics was tested by the three-point bending method using an electronic universal testing machine (ETM305F-2, WANCE, China) (Pan et al., 2020). The loading speed was kept at 0.5 mm/min and span at 40 mm.

RESULTS AND DISCUSSION

Phase Composition, Relative Content, and Structural Distortion of EBFS Ceramics

As shown in **Figure 1** and **Table 1**, the samples sintered at 1,000–1,150°C underwent significant changes in their phase composition and contents. For instance, the ceramic treated at 1,000°C (EBFS-1000) was composed of the gehlenite, diopside, perovskite, and rutile phases. An increase to 1,100°C (EBFS-1100) caused the transformation of gehlenite into akermanite, which was associated with a MgO/Al_2O_3 ratio > 0.55 (Wang et al., 2017). In turn, diopside transformed into Fe-bearing diopside, as seen from the downshift of the characteristic diffraction peaks of diopside (from 2θ = 29.94, 35.22°, and 35.76° to 2θ = 29.86°, 35.12°, and 35.70°, respectively). This was related to the high-temperature partial replacement of Mg^{2+} ions with Fe^{2+} cations at the octahedral positions or Fe^{3+} ions for the Si^{4+} cations at the tetrahedral position (Chen et al., 2019). In this respect, the diffraction peaks emerged at 2θ = 45.90°, 52.74°, and 60.20° are attributed to (−1 3 2), (−1 1 3), and (−6 0 2) crystal planes of the Fe-bearing diopside, respectively. Besides the existence of Fe-bearing diopside, this proved the disappearance of rutile, whose reactions with Ca^{2+} and free oxygen O^{2-} ions induced the formation of a perovskite phase:

$$Ca^{2+} + TiO_2 + O^{2-} = CaTiO_3 \quad (4)$$

Once the sintering temperature reached a value of 1,150°C (EBFS-1150), the magnesium–aluminum spinel was formed. In this case, the Mg^{2+} cations, being apart from the phase formation or substituted by the Fe^{2+} ions, combined with Al^{3+} and free oxygen O^{2-} ions to form the $MgAl_2O_4$ phase, as shown by Eq. 5:

$$Mg^{2+} + 2Al^{3+} + 4O^{2-} = MgAl_2O_4 \quad (5)$$

At the sintering temperatures of 1,150–1,200°C, the phase composition of the samples remained unchanged, but the relative content of each phase was different. An increase in the sintering temperature promoted the formation of magnesium–aluminum spinel grains and their growth, leading to a constant rise in the relative magnesium–aluminum spinel content (Bessa et al., 2019). In turn, a decrease in the thermal stability of a perovskite structure within the same temperature range causes a reduction of 1.8% in its relative content (Lyubenova et al., 2009; Jiang et al., 2015). The relative content of Fe-bearing diopside first increased and then decreased, whereas akermanite exhibited the opposite trend. This was due to the poor thermal stability of Fe-bearing diopside grains and the secondary growth of akermanite grains (Tulyaganov et al., 2002). **Table 2** shows the refinement factors and R/E, and the good refinement of the obtained XRD results was confirmed by the R/E values ranging from 1.29 to 1.87.

Table 3 shows the unit cell variations of Fe-bearing diopside and magnesium–aluminum spinel. An increase in the cell volume for both crystalline phases indicates the grain growth with increasing sintering temperature. Furthermore, the extended a- and c-axes of the Fe-bearing diopside along with a shortened b-axis reveal the predominant a- and c-axis orientation of the grains of this phase. Besides, an increase in β-angle, followed by its decrease, evidences the structural distortion upon the grain growth, which is mainly caused by ion substitution and indicates the poor high-temperature stability of Fe-bearing diopside. In this case, ion substitution provokes an increase in a cell

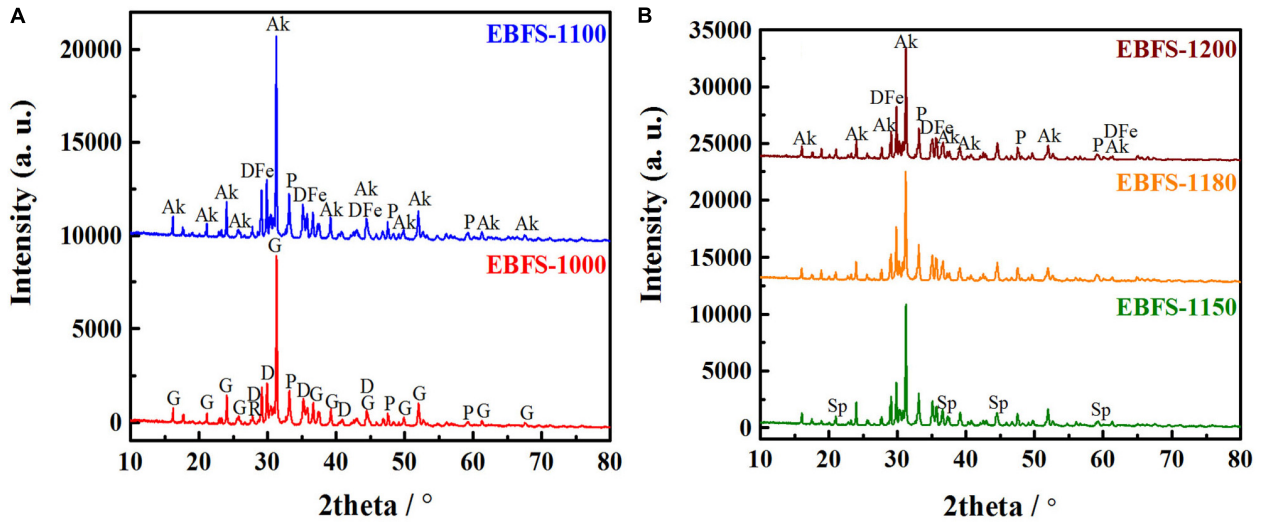

FIGURE 1 | X-ray powder diffraction patterns of EBFS ceramics at different sintering temperatures: **(A)** 1,000 and 1,100°C, **(B)** 1,150, 1,180, and 1,200°C (Ak, Akermanite; D, Diopside; P, Perovskite; G, Gehlenite; R, Rutile; DFe, Fe-bearing Diopside; Sp, Spinel).

TABLE 1 | Relative contents of crystalline phases in EBFS ceramics.

Samples	Relative contents of phases (%)						
	Gehlenite	Diopside	Fe-bearing diopside	Perovskite	Rutile	Akermanite	Spinel
EBFS-1000	51.0 (3.0)	39.6 (1.8)	–	9.2 (0.4)	0.2 (0.1)	–	–
EBFS-1100	–	11.9 (1.5)	25.3 (2.3)	9.8 (0.4)	–	52.9 (3.6)	–
EBFS-1150	–	–	36.3 (2.6)	10.8 (0.3)	–	50.6 (1.4)	2.3 (0.6)
EBFS-1180	–	–	38.9 (2.6)	10.2 (0.3)	–	42.1 (1.2)	8.7 (1.2)
EBFS-1200	–	–	37.1 (2.6)	9.0 (0.3)	–	44.5 (1.2)	9.4 (1.2)

TABLE 2 | Refinement factors and R/E values of EBFS ceramics.

Samples	R-factors	E-factors	R/E
EBFS-1000	0.0883	0.0532	1.66
EBFS-1100	0.0879	0.0509	1.73
EBFS-1150	0.0924	0.0495	1.87
EBFS-1180	0.0605	0.0480	1.26
EBFS-1200	0.0642	0.0497	1.29

defect concentration, which is beneficial for the capture of photogenerated electrons (Huang et al., 2016; Isari et al., 2018; Safari et al., 2020).

An increase in a-, b-, and c-axis lengths of the magnesium–aluminum spinel means a simultaneous grain growth along the three dimensions, keeping $\alpha = \beta = \gamma = 90°$ constant with temperature. This indicates the cell structure stability of the magnesium–aluminum spinel at high temperatures. According to the works by Li et al. (2011, 2016), the magnesium–aluminum spinel nanoparticles synthesized at temperatures from 700 to 1,000°C possess good photocatalytic performance. However, in this experiment, the magnesium–aluminum spinel phase was obtained at temperatures above 1,150°C and was composed of micro-scaled grains. Therefore, the magnesium–aluminum spinel does not contribute to the photocatalytic performance of the samples.

Appearance, Microstructure, and Physical Properties of EBFS Ceramics

Figure 2 shows the appearance of EBFS ceramic samples. An increase in the sintering temperature caused a color change of the sample surface from light yellow to brown. Furthermore, the EBFS-1200 sample reveals a few bubbles on its surface, whereas other samples are flat.

Figure 3 depicts the scanning electron microscope (SEM) optical micrographs of EBFS ceramics. It is obvious that an increase in the sintering temperatures can effectively reduce the degree of porosity: while the structure of EBFS-1000–EBFS-1150 samples is full of large and interconnected pores, the EBFS-1180 ceramic evidences only a few tiny and isolated pores with a liquid phase filling the gaps between the grains and thus improving the compactness of this specimen in comparison with others. As for the EBFS-1200 sample, its surface was found to be dense (**Figure 3E**), but the interior was loose (**Figure 3F**). In this case, the liquid phase

TABLE 3 | Cell parameters and volumes of Fe-bearing diopside and spinel.

Phase	Samples	a (Å)	b (Å)	c (Å)	V (Å^3)	α (°)	β (°)	γ (°)
Fe-bearing diopside	EBFS-1150	9.73221	8.83962	5.31166	439.0	90.0	106.101	90.0
	EBFS-1180	9.75045	8.83023	5.32362	440.4	90.0	106.082	90.0
	EBFS-1200	9.76877	8.83103	5.33859	442.5	90.0	106.080	90.0
Spinel	EBFS-1150	8.10617	8.10617	8.10617	532.7	90.0	90.0	90.0
	EBFS-1180	8.11269	8.11269	8.11269	533.9	90.0	90.0	90.0
	EBFS-1200	8.11821	8.11821	8.11821	535.0	90.0	90.0	90.0

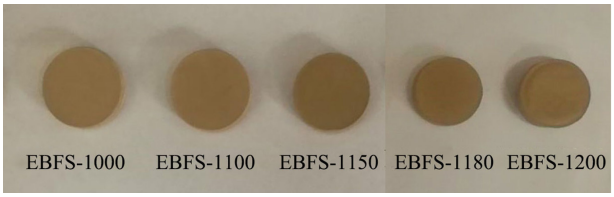

FIGURE 2 | Appearance of EBFS ceramics.

generated at a high temperature was easier to flow on the surface of the sample, resulting in a more dense surface. Meanwhile, remelting or growth of some grains broke down the internal structure, leading to the emergence of "closed pores," which could deteriorate the compactness of ceramic samples (Liu et al., 2016).

Figure 4 displays the EDS results obtained on different morphological grains at points referred to as A, B, C, and D in the EBFS-1180 sample. According to the EDS spectra acquired at these points, each of them is associated with diverse types of mineral phases. A comparative analysis of EDS data with the XRD analysis reveals that point A with short columnar grains refers to akermanite, point B with octahedral conical grains is associated with a magnesium–aluminum spinel phase, point C with bulk grains is attributed to Fe-bearing diopside, and point D with irregular grains is due to a perovskite structure. In addition, the elemental distribution at each point enables one to conclude that the formed phases are variably affected by ion substitution, and the strongest impact is observed for Fe-bearing diopside and perovskite phases. In addition, for a more comprehensive demonstration of the correspondence between crystalline phases and morphological grains, EDS mapping results of the EBFS-1180 sample are provided in **Supplementary Figure 1**.

Table 4 shows the physical properties of EBFS ceramics. Generally, with increasing sintering temperatures, the linear shrinkage rate, bulk density, and bending strength of ceramic samples followed a "decrease–increase–decrease" process, while the water absorption increased first and then decreased. EBFS-1180 ceramic showed the best physical properties with the largest linear shrinkage rate, elevated bulk density, and superior bending strength, and the water absorption was at a low level. Combined with **Figure 3**, it can be seen that the structural denseness of EBFS ceramics is positively correlated with the physical properties, that is, the better its denseness, the higher its physical properties.

Light Absorption Capacity of EBFS Ceramics

Figure 5A shows UV-Vis spectra of EBFS ceramics. As seen, the absorbance of ceramic samples in the UV region first increased and then decreased with a rising sintering temperature. Since the gehlenite, akermanite, and diopside phases have the low light absorption capability, the absorbance of EBFS-1000 sample in the UV and visible regions was mainly due to rutile. In turn, the decrease of the rutile content in EBFS-1100 ceramic reduced the absorbance in the UV range; furthermore, the diopside phase partly transformed into Fe-bearing diopside, resulting in the redshift of the absorption edge and thus enhancing the light absorption in the visible region of the sample (Yang et al., 2012). In the case of EBFS-1150 sample, a precipitous increase in the absorbance within the UV and visible regions along with a continuous redshift of the absorption edge was associated with a rising Fe-bearing diopside content, the highest amount of a perovskite phase, and the emergence of a magnesium–aluminum spinel phase (Lei and Xue, 2008a; Yang et al., 2012; Rahman and Jayaganthan, 2015). For ceramics sintered at temperatures from 1,150 to 1,200°C, a dramatic decrease of absorbance was consistent with the XRD results, revealing a decrease in the perovskite content and an increase in the magnesium–aluminum spinel phase concentration. **Figure 5B** displays the corresponding first-derivative curves of the UV-Vis spectra for EBFS-1100–EBFS-1200 samples, where the strongest peaks corresponded to the wavelengths of 376, 360.5, 358.5, 327, and 419 nm, respectively. The relevant bandgap energies were calculated using Eq. 6 from the works of Li et al. (2011) and Yan et al. (2018):

$$E_g = 1240/\lambda \quad (6)$$

where *Eg* is the bandgap (eV) and λ is the wavelength at the corresponding strongest peak (nm). These were found to be 3.30, 3.44, 3.46, 3.79, and 2.96 eV, respectively, thus covering the UV-range and reflecting the ability of the obtained EBFS ceramics to absorb the active solar energy (3.97 eV) released during the photocatalytic process (Kwon et al., 2020).

Photocatalytic Performance of EBFS Ceramics

Effect of pH

To investigate the effect of pH on the photocatalytic performance, the degradation rate of RhB with different pH levels was tested by the example of EBFS-1180 sample (**Figure 6**). The dense

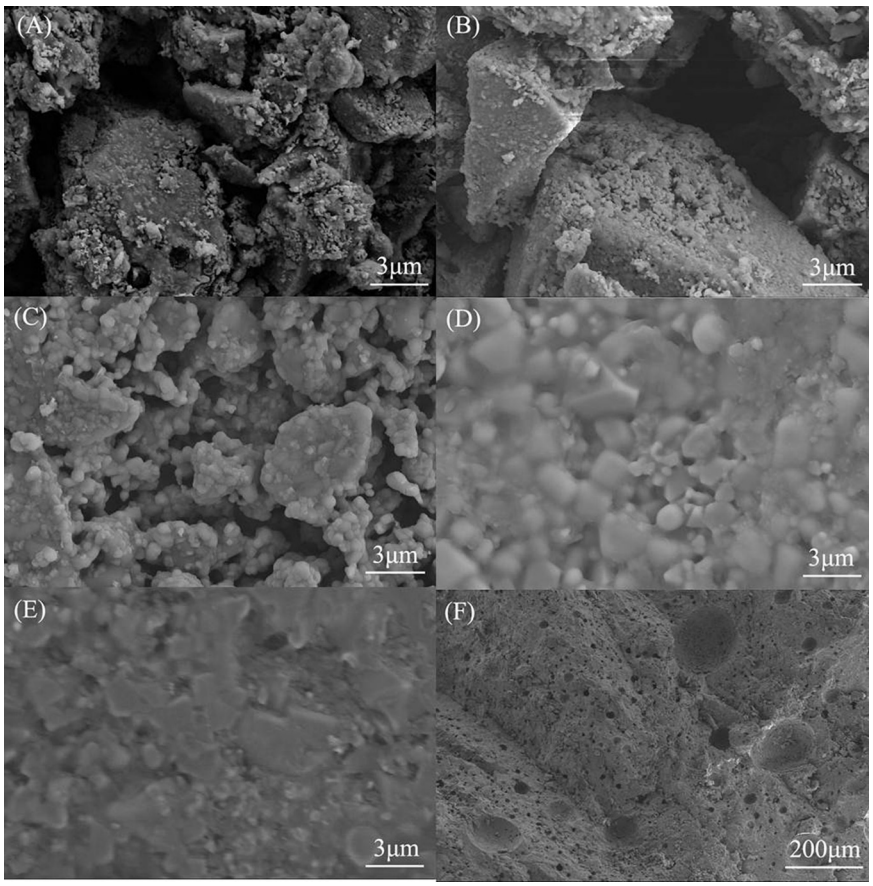

FIGURE 3 | Scanning electron microscope images of EBFS ceramics: **(A)** EBFS-1000, **(B)** EBFS-1100, **(C)** EBFS-1150, **(D)** EBFS-1180, **(E)** EBFS-1200a, and **(F)** EBFS-1200b.

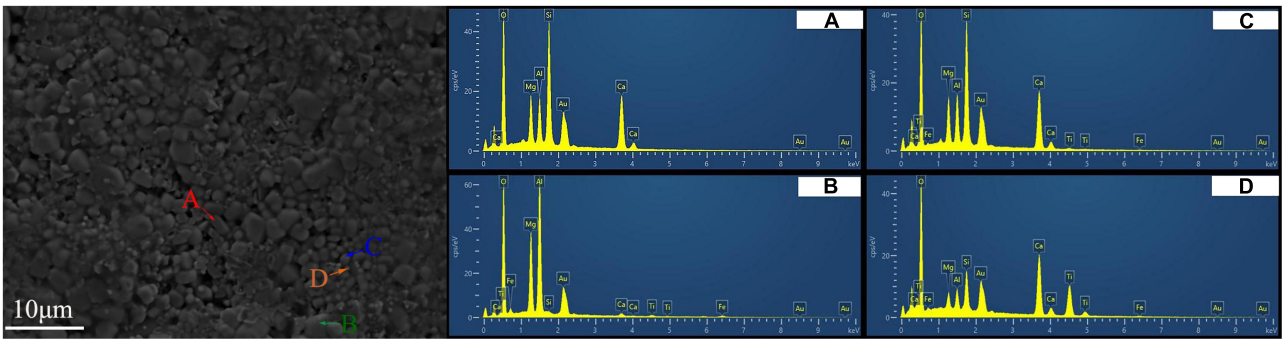

FIGURE 4 | Energy dispersive spectrometer images of EBFS-1180 ceramic.

microstructure of EBFS-1180 sample was beneficial to resist acid or alkali corrosion. While the pH increased from 1 to 5, the degradation rate first increased and then decreased. At pH = 5, the degradation rate was 0%, reaching the highest value (77%) at pH = 2. Hence, EBFS-1180 ceramic exhibits good photocatalytic activity within a pH range of about 1–2.5, which is similar to photo-Fenton and photo-Fenton-like catalysts (pH = 2–3) (Ebrahiem et al., 2017; Zhu et al., 2018), but much lower than for semiconductor photocatalysts like titanium dioxide (pH = 6–11) (Isari et al., 2018; Sirirerkratana et al., 2019). The reason for this may be as follows: at a relatively high level of acidity, there is a large number of OH- anions in the solution, which could accelerate the scavenging of OH radicals, having a detrimental effect on the photocatalytic reaction. In turn, at a relatively low pH, the combination of H^+ cations with O^{2-} anions in the solution generates H_2O_2, degrading the pollutant.

TABLE 4 | Physical properties of EBFS ceramics.

Samples	Linear shrinkage rate (%)	Bulk density (g/cm^3)	Water absorption (%)	Bending strength (MPa)
EBFS-1000	−1.71 ± 0.05	1.64 ± 0.02	29.31 ± 0.75	2.69 ± 0.04
EBFS-1100	−1.03 ± 0.08	1.67 ± 0.01	28.18 ± 0.22	3.20 ± 0.32
EBFS-1150	2.58 ± 0.25	1.86 ± 0.03	22.66 ± 0.86	14.09 ± 0.95
EBFS-1180	14.47 ± 0.29	2.81 ± 0.04	0.53 ± 0.20	44.53 ± 1.26
EBFS-1200	12.96 ± 1.09	2.32 ± 0.03	0.24 ± 0.09	40.83 ± 0.92

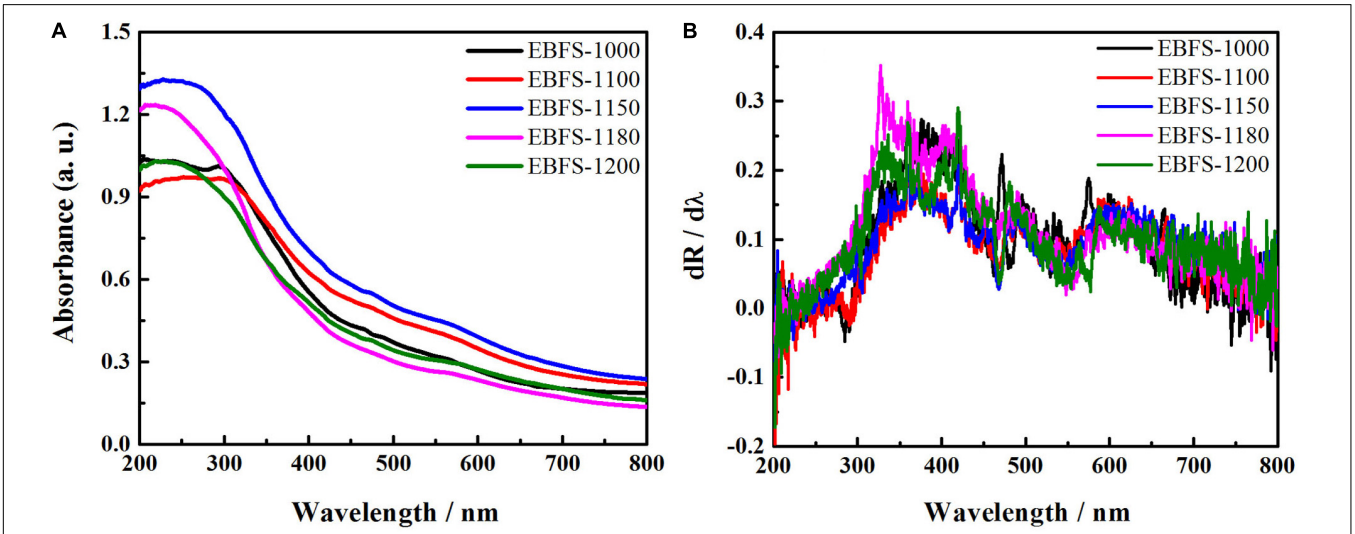

FIGURE 5 | (A) UV-Vis spectra of EBFS ceramics and **(B)** the corresponding first-derivative curves of the UV-Vis spectra.

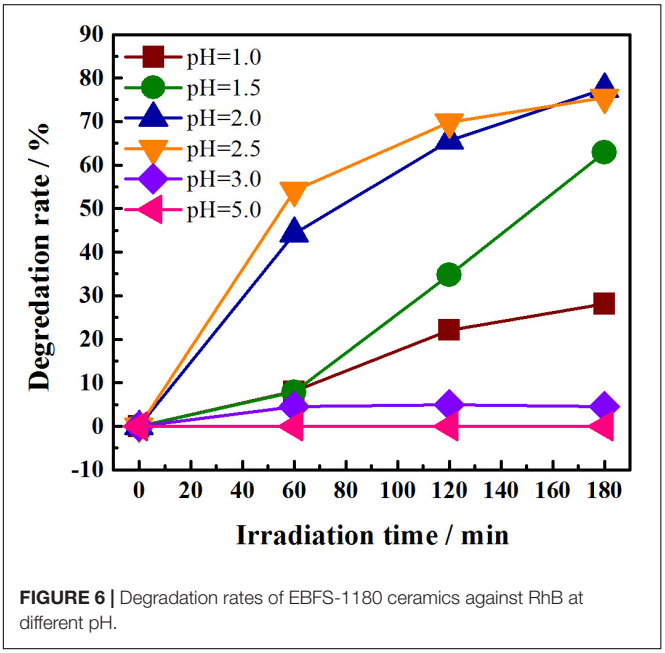

FIGURE 6 | Degradation rates of EBFS-1180 ceramics against RhB at different pH.

To further investigate the performance of EBFS-1180 ceramic in an acidic environment and determine its suitability as a ceramic catalyst, the sample was immersed for 24 h in an acidic solution with pH = 2. Its corrosion rate was measured afterward to be only 0.03%, evidencing that EBFS-1180 is able to catalyze the degradation of pollutants in an acidic environment.

Effect of Sintering Temperature

Figure 7 displays the photocatalytic degradation rates of EBFS ceramics prepared at different sintering temperatures against the RhB solution at pH = 2. At 1,000°C, the degradation rate was almost 0%, indicating that EBFS-1000 sample was photocatalytically inactive. At 1,100°C, the degradation rate reached 18%, meaning that EBFS-1100 specimen possessed the initial photocatalytic activity, which was mainly related to the partial transformation of diopside into an Fe-bearing diopside phase (Yang et al., 2012). At 1,150°C, the degradation rate rose to 50%, showing that diopside was completely transformed into Fe-bearing diopside, and the crystalline structure of EBFS-1150 sample reached stability.

The best photocatalytic performance was provided by EBFS-1180 ceramic, whose degradation rate achieved 77% within 180 min. Such a drastic increase in the photocatalytic activity could be owing to the following reasons. First, the liquid phase generated during the sintering process accelerated the electron transfer (Bernardo et al., 2010). Second, the "occlusal" morphology formed among the grains (**Figure 3D**), which shortened the electron migration path. Third, the relative Fe-bearing diopside content reached the highest value. Meanwhile, the ion substitution led to an increase in the degree of cell distortion and the defect concentration (Tulyaganov et al., 2002),

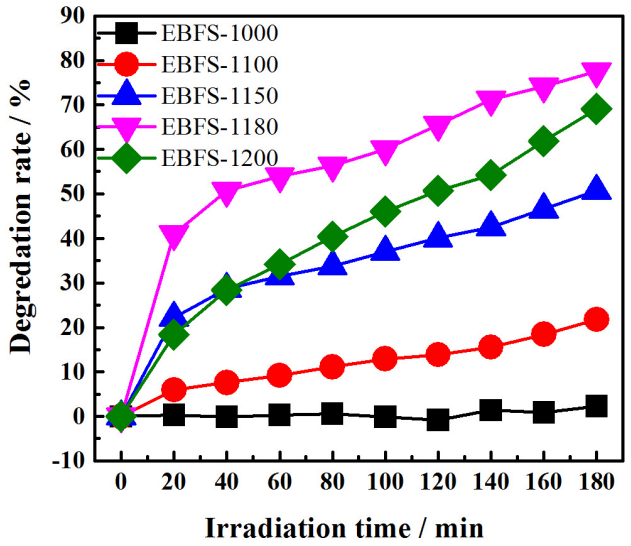

FIGURE 7 | Degradation rates of EBFS ceramics against RhB at pH = 2.

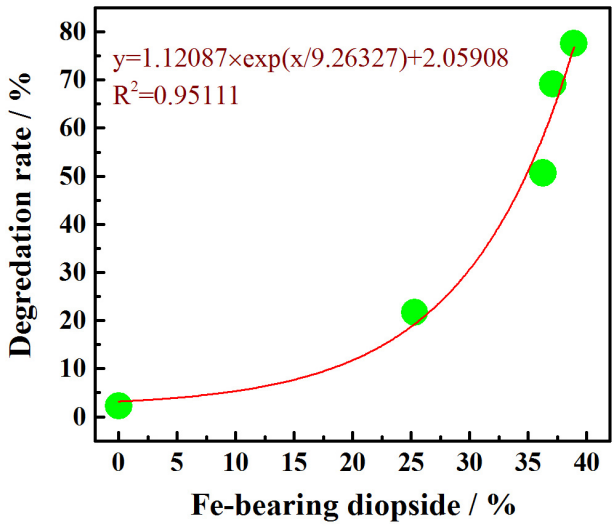

FIGURE 8 | Fe-bearing diopside contents versus degradation rates.

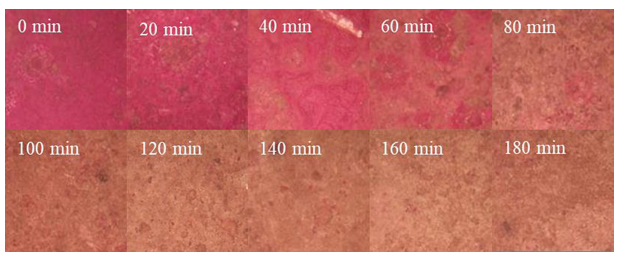

FIGURE 9 | Rhodamine B spots on the surface of EBFS-1180 ceramic at different irradiation time.

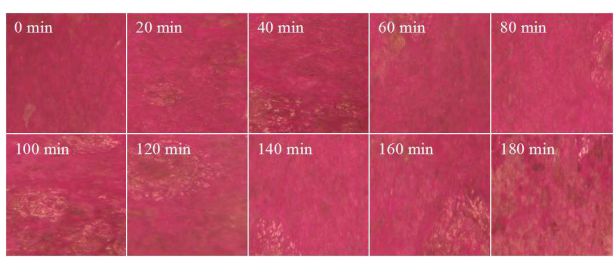

FIGURE 10 | Rhodamine B spots on the surface of EBFS-1180 ceramic without light irradiation.

causing the emergence of bulk surface vacancies (Huang et al., 2016). These vacancies can be used to capture the electrons generated by the decomposition of RhB and improve the degradation efficiency of the latter. To better show the photocatalytic performance of EBFS-1180 and the variation of RhB during photocatalytic degradation, as shown in **Supplementary Figure 2**, the strongest absorption peak height of RhB on the spectral curves gradually decreased with an increasing irradiation time, indicating that the degradation ability of EBFS-1180 against RhB gradually increased. Meanwhile, that peak was obviously blue-shifted from 554 nm, which is due to the generation of de-N-ethyl intermediates with the reaction group during the degradation of RhB (Li et al., 2019). At 1,200°C, the degradation rate decreased to 69% at a relative Fe-bearing diopside content drop. Furthermore, the destruction of a dense structure resulted in the deterioration of the photocatalytic efficiency. Therefore, there was the direct relation between the relative Fe-bearing diopside content and the degradation rate.

In this respect, **Figure 8** shows the degradation rate as a function of Fe-bearing content, properly described by a non-linear equation $y = 1.12087 \times \exp(x / 9.26327) + 2.05908$, where y is the degradation rate (%) and x is the relative content of the Fe-bearing diopside (%). The R^2 value of 0.95111 is the goodness-of-fit indicator.

RhB Layer Degradation

The photocatalytic performance of an EBFS-1180 bulk sample was tested afterward via the RhB layer degradation in accordance to Section "Photocatalytic Performance" to assess the suitability of this ceramic for practical application. According to the microscopic analysis, under UV light irradiation, the RhB spots on the surface of a bulk sample faded gradually (**Figure 9**), while without UV light irradiation, the RhB spots did little change (**Figure 10**). It was thereby shown that RhB was effectively degraded under the UV light irradiation and the degradation rate increased with irradiation time.

CONCLUSION

Photocatalytic ceramics were prepared by powder sintering at different temperatures using EBFS. At 1,000–1,150°C, ceramics revealed the dramatic change in their phase composition. At 1,150–1,200°C, the phase composition of ceramics remained

unchanged, but there were variations in the relative content of each component. In particular, the amount of magnesium–aluminum spinel increased from 2.3 to 9.4%, the perovskite concentration decreased from 10.8 to 9.0%, and the quantity of akermanite first decreased and then increased, whereas the diopside demonstrated the opposite trend. Furthermore, ceramics sintered at 1,150–1,200°C exhibited a gradual grain growth. For example, Fe-bearing diopside grains mainly grew along the a- and c-axes, and the magnesium–aluminum spinel grains evolved simultaneously along the a-, b-, and c-axes.

The best compactness was found in EBFS-1180 sample, where the liquid phase "intercalated" into the grains. According to the SEM and EDS data, EBFS-1180 ceramic was composed of short columnar grains of akermanite, octahedral conical grains of magnesium–aluminum spinel, bulk grains of Fe-bearing diopside, and irregular grains of perovskite.

The absorbance of EBFS ceramic samples in the UV region first increased and then decreased with an increasing sintering temperature. Within a temperature range of 1,150–1,200°C, the decrease in absorbance was mainly due to a decrease in the perovskite phase content and an increase in the magnesium–aluminum spinel concentration.

Ti-extraction blast furnace slag-1180 sample was found to possess good photocatalytic performance in acidic medium (pH = 1–3). For instance, its RhB degradation rate enriched 77% at pH = 2 within 180 min of the UV light irradiation. Furthermore, a non-linear relationship was established between the degradation of RhB and the relative Fe-bearing diopside content in ceramics.

The prolonged UV irradiation time led to a gradual fading of RhB spots on the surface of EBFS-1180 bulk ceramic and a progressive increase in their degradation rate. In addition, the corrosion rate of EBFS-1180 sample after immersion for 24 h in an acidic solution (pH = 2) was only 0.03%, indicating that EBFS-1180 sample is a promising ceramic catalyst for the degradation of pollutants in an acidic environment.

DATA AVAILABILITY STATEMENT

The original contributions presented in the study are included in the article/**Supplementary Material**, further inquiries can be directed to the corresponding author/s.

AUTHOR CONTRIBUTIONS

HY and YL contributed to the conceptualization, methodology, experiment, data analysis, and manuscript preparation. HS and TP contributed to the investigation, formal analysis, and manuscript review. All authors have read and approved the content of the manuscript.

SUPPLEMENTARY MATERIAL

The Supplementary Material for this article can be found online at: https://www.frontiersin.org/articles/10.3389/fmats.2021.652009/full#supplementary-material

Supplementary Figure 1 | Energy dispersive spectrometer mappings of the EBFS-1180 ceramic.

Supplementary Figure 2 | UV–vis absorption spectra of photocatalytic degradation of RhB by EBFS-1180 ceramic.

REFERENCES

Bernardo, E., Bonomo, E., and Dattoli, A. (2010). Optimisation of sintered glass–ceramics from an industrial waste glass. *Ceram. Int.* 36, 1675–1680. doi: 10.1016/j.ceramint.2010.02.047

Bessa, L. P., Ferreira, E. D. P., Magalhães, F. D. S., Ferreira, F. B., Cardoso, V. L., and Reis, M. H. M. (2019). Micro-structured and reinforced spinel hollow fiber membranes: influence of sintering temperature and ceramic powder composition. *Ceram. Int.* 45, 23632–23642. doi: 10.1016/j.ceramint.2019.08.075

Chen, H., Li, B., Zhao, M., Zhang, X., Du, Y., Shi, Y., et al. (2019). Lanthanum modification of crystalline phases and residual glass in augite glass ceramics produced with industrial solid wastes. *J. Non Cryst. Solids* 524:119638. doi: 10.1016/j.jnoncrysol.2019.119638

Ebrahiem, E. E., Al-Maghrabi, M. N., and Mobarki, A. R. (2017). Removal of organic pollutants from industrial wastewater by applying photo-Fenton oxidation technology. *Arab. J. Chem.* 10, S1674–S1679. doi: 10.1016/j.arabjc.2013.06.012

He, S., Peng, T., and Sun, H. (2019a). Titanium recovery from Ti-bearing blast furnace slag by alkali calcination and acidolysis. *JOM* 71, 3196–3201. doi: 10.1007/s11837-019-03575-9

He, S., Peng, T., Sun, H., Luo, D., Xiao, Q., and Geng, Q. (2019b). Kinetics of iron removal from ti-extraction blast furnace slag by chlorination calcination. *Open Chem.* 17, 1146–1156. doi: 10.1515/chem-2019-0124

Hou, H., Zhou, J., Ji, M., Yue, Y., Qian, G., and Zhang, J. (2020). Mechanochemical activation of titanium slag for effective selective catalytic reduction of nitric oxide. *Sci. Total Environ.* 743:140733. doi: 10.1016/j.scitotenv.2020.140733

Huang, X., Yan, X., Wu, H., Fang, Y., Min, Y., Li, W., et al. (2016). Preparation of Zr-doped $CaTiO_3$ with enhanced charge separation efficiency and photocatalytic activity. *Trans. Nonferrous Metals Soc. Chin.* 26, 464–471. doi: 10.1016/S1003-6326(16)64097-9

Isari, A. A., Payan, A., Fattahi, M., Jorfi, S., and Kakavandi, B. (2018). Photocatalytic degradation of rhodamine B and real textile wastewater using Fe-doped TiO_2 anchored on reduced graphene oxide (Fe-TiO_2/rGO): characterization and feasibility, mechanism and pathway studies. *Appl. Surf. Sci.* 462, 549–564. doi: 10.1016/j.apsusc.2018.08.133

Jiang, J., Fang, D., Lu, C., Dou, Z., Wang, G., Zhang, F., et al. (2015). Solid-state reaction mechanism and microwave dielectric properties of $CaTiO_3$–$LaAlO_3$ ceramics. *J. Alloys Compd.* 638, 443–447. doi: 10.1016/j.jallcom.2015.03.073

Kwon, O., Takahashi, Y., Miyazaki, T., Terakado, N., and Fujiwara, T. (2020). Nanostructure and photocatalytic behavior of glass-ceramics in Bi_2O_3–Nb_2O_5–Li_2O–B_2O_3–SiO_2 system. *J. Ceram. Soc. Jpn.* 128, 839–842. doi: 10.2109/jcersj2.20125

Lei, X. F., and Xue, X. X. (2008a). Preparation and characterization of perovskite-type Titania-bearing blast furnace slag photocatalyst. *Mater. Sci. Semicond. Process.* 11, 117–121. doi: 10.1016/j.mssp.2009.05.002

Lei, X. F., and Xue, X. X. (2008b). Preparation of perovskite type titanium-bearing blast furnace slag photocatalyst doped with sulphate and investigation on reduction Cr(VI) using UV–vis light. *Mater. Chem. Phys.* 112, 928–933. doi: 10.1016/j.matchemphys.2008.06.065

Lei, Y., Sun, L., Ma, W., Ma, X., Wu, J., Li, S., et al. (2018). An approach to employ titanium-bearing blast-furnace slag to prepare Ti and Al–Si alloys. *J. Alloys Compd.* 769, 983–990. doi: 10.1016/j.jallcom.2018.08.077

Li, F., Zhao, Y., Liu, Y., Hao, Y., Liu, R., and Zhao, D. (2011). Solution combustion synthesis and visible light-induced photocatalytic activity of mixed amorphous and crystalline $MgAl_2O_4$ nanopowders. *Chem. Eng. J.* 173, 750–759. doi: 10.1016/j.cej.2011.08.043

Li, H., Liu, Y., Tang, J., and Deng, Y. (2016). Synthesis, characterization and photocatalytic properties of $Mg_{1-x}Zn_xAl_2O_4$ spinel nanoparticles. *Solid State Sci.* 58, 14–21. doi: 10.1016/j.solidstatesciences.2016.05.007

Li, Y., Sun, H., Peng, T., You, H., Qin, Y., and Zeng, L. (2019). Effects of muscovite matrix on photocatalytic degradation in TiO_2/muscovite nanocomposites. *Appl. Clay Sci.* 179:105155. doi: 10.1016/j.clay.2019.105155

Liu, T., Tang, Y., Li, Z., Wu, T., and Lu, A. (2016). Red mud and fly ash incorporation for lightweight foamed ceramics using lead-zinc mine tailings as foaming agent. *Mater. Lett.* 183, 362–364. doi: 10.1016/j.matlet.2016.07.041

Lyubenova, T. S., Matteucci, F., Costa, A. L., Dondi, M., Ocaña, M., and Carda, J. (2009). Synthesis of Cr-doped $CaTiSiO_5$ ceramic pigments by spray drying. *Mater. Res. Bull.* 44, 918–924. doi: 10.1016/j.materresbull.2008.08.009

Pan, Y., Li, H., Liu, Y., Liu, Y., Hu, K., Wang, N., et al. (2020). Effect of holding time during sintering on microstructure and properties of 3D printed alumina ceramics. *Front. Mater.* 7:54. doi: 10.3389/fmats.2020.00054

Rahman, A., and Jayaganthan, R. (2015). Study of photocatalyst magnesium aluminate spinel nanoparticles. *J. Nanostructure Chem.* 5, 147–151. doi: 10.1007/s40097-014-0135-9

Rezvani, M., Eftekhari-Yekta, B., Solati-Hashjin, M., and Marghussian, V. K. (2005). Effect of Cr_2O_3, Fe_2O_3 and TiO_2 nucleants on the crystallization behaviour of SiO_2-Al_2O_3-CaO-MgO(R_2O) glass-ceramics. *Ceram. Int.* 31, 75–80. doi: 10.1016/j.ceramint.2004.03.037

Safari, S., Seyed Ahmadian, S. M., and Amani-Ghadim, A. R. (2020). Visible light photocatalytic activity enhancing of $MTiO_3$ perovskites by M cation (M = Co, Cu, and Ni) substitution and Gadolinium doping. *J. Photochem. Photobiol. A* 394:112461. doi: 10.1016/j.jphotochem.2020.112461

Sirirerkratana, K., Kemacheevakul, P., and Chuangchote, S. (2019). Color removal from wastewater by photocatalytic process using titanium dioxide-coated glass, ceramic tile, and stainless steel sheets. *J. Clean. Prod.* 215, 123–130. doi: 10.1016/j.jclepro.2019.01.037

Tulyaganov, D. U., Ribeiro, M. J., and Labrincha, J. A. (2002). Development of glass-ceramics by sintering and crystallization of fine powders of calcium-magnesium-aluminosilicate glass. *Ceram. Int.* 28, 515–520. doi: 10.1016/S0272-8842(02)00004-4

Wang, H., Ding, B., Zhu, X., Tan, Y., He, X., and Liao, Q. (2017). Influence of Al_2O_3 content on crystallization behaviors of blast furnace slags in directional solidification process. *Int. J. Heat Mass Transfer* 113, 286–294. doi: 10.1016/j.ijheatmasstransfer.2017.05.020

Wang, J., Sen, S., Yu, P., Browning, N. D., and Kauzlarich, S. M. (2010). Synthesis and spectroscopic characterization of P-doped Na_4Si_4. *J. Solid State Chem.* 183, 2522–2527. doi: 10.1016/j.jssc.2010.07.051

Xi, C., Zheng, F., Xu, J., Yang, W., Peng, Y., Li, Y., et al. (2018). Preparation of glass-ceramic foams using extracted titanium tailing and glass waste as raw materials. *Constr. Build. Mater.* 190, 896–909. doi: 10.1016/j.conbuildmat.2018.09.170

Xi, C., Zhou, J., Zheng, F., Gao, J. M., Hu, P., Li, Y., et al. (2020). Conversion of extracted titanium tailing and waste glass to value-added porous glass ceramic with improved performances. *J. Environ. Manage.* 261:110197. doi: 10.1016/j.jenvman.2020.110197

Yan, Y., Yang, H., Zhao, X., Li, R., and Wang, X. (2018). Enhanced photocatalytic activity of surface disorder-engineered $CaTiO_3$. *Mater. Res. Bul.* 105, 286–290. doi: 10.1016/j.materresbull.2018.05.008

Yang, H., Xue, X., Zuo, L., and Yang, Z. (2004). Photocatalytic degradation of methylene blue with blast fumace slag containing titania. *The Chin. J. Process Eng.* 4, 265–268. doi: 10.3321/j.issn:1009-606X.2004.03.014

Yang, H., Yang, Z.-J., Han, C., Li, Q., and Xue, X.-X. (2012). Photocatalytic activity of Fe-doped diopside. *Trans. Nonferrous Metals Soc. Chin.* 22, 3053–3058. doi: 10.1016/s1003-6326(11)61570-7

You, H., Sun, H., Peng, T., Li, Y., Zeng, L., and Qin, Y. (2020). Effect of sintering time on crystal and structure of chlorine-containing low-titanium slag glass-ceramics. *IOP Conf. Ser. Earth Environ. Sci.* 615:012124. doi: 10.1088/1755-1315/615/1/012124

Zhang, G., Yan, Y., Hu, Z., and Xiao, B. (2017). Investigation on preparation of pyrite tailings-based mineral admixture with photocatalytic activity. *Constr. Build. Mater.* 138, 26–34. doi: 10.1016/j.conbuildmat.2017.01.134

Zhang, J., Yan, Y., and Hu, Z. (2018). Preparation and characterization of foamed concrete with Ti-extracted residues and red gypsum. *Constr. Build. Mater.* 171, 109–119. doi: 10.1016/j.conbuildmat.2018.03.072

Zhang, J., Yan, Y., Hu, Z., Xie, X., and Yang, L. (2019). Properties and hydration behavior of Ti-extracted residues-red gypsum based cementitious materials. *Constr. Build. Mater.* 218, 610–617. doi: 10.1016/j.conbuildmat.2019.05.099

Zhao, L., Li, Y., Zhou, Y., and Cang, D. (2014). Preparation of novel ceramics with high CaO content from steel slag. *Mater. Design* 64, 608–613. doi: 10.1016/j.matdes.2014.08.015

Zhao, W., and Tan, W. (2018). Quantitative and structural analysis of minerals in soil clay fractions developed under different climate zones in China by XRD with Rietveld method, and its implications for pedogenesis. *Appl. Clay Sci.* 162, 351–361. doi: 10.1016/j.clay.2018.05.019

Zhu, Y., Zhu, R., Yan, L., Fu, H., Xi, Y., Zhou, H., et al. (2018). Visible-light Ag/AgBr/ferrihydrite catalyst with enhanced heterogeneous photo-Fenton reactivity via electron transfer from Ag/AgBr to ferrihydrite. *Appl. Catal. B Environ.* 239, 280–289. doi: 10.1016/j.apcatb.2018.08.025

Conflict of Interest: The authors declare that the research was conducted in the absence of any commercial or financial relationships that could be construed as a potential conflict of interest.

Publisher's Note: All claims expressed in this article are solely those of the authors and do not necessarily represent those of their affiliated organizations, or those of the publisher, the editors and the reviewers. Any product that may be evaluated in this article, or claim that may be made by its manufacturer, is not guaranteed or endorsed by the publisher.